Cold sprayed WC reinforced maraging steel 300 composites: Microstructure characterization and mechanical properties

Chaoyue Chen, Yingchun Xie, Xincheng Yan, Renzhong Huang, Min Kuang, Wenyou Ma, Ruixin Zhao, Jiang Wang, Min Liu, Zhongming Ren, et al.

Cold sprayed WC reinforced maraging steel 300 composites: microstructure characterization and mechanical properties

Chaoyue Chen[a, b], Yingchun Xie[c*], Xincheng Yan[b, c*], Renzhong Huang[c], Min Kuang[c], Wenyou Ma[c], Ruixin Zhao[a], Jiang Wang[a*], Min Liu[c], Zhongming Ren[a], Hanlin Liao[b]

a) *State Key Laboratory of Advanced Special Steels, School of Materials Science and Engineering, Shanghai University, Shanghai 200072, China*

b) *ICB UMR 6303, CNRS, Univ. Bourgogne Franche-Comté, UTBM, F-90010 Belfort, France*

c) *National Engineering Laboratory for Modern Materials Surface Engineering Technology; The Key Lab of Guangdong for Modern Surface Engineering Technology; Guangdong Institute of New Materials, Guangzhou 510651, P.R. China*

Abstract: Maraging steel 300 (MS300) is a precipitation-strengthening iron–nickel alloy with outstanding properties such as good mechanical strength, weldability and corrosion resistance. However, the poor wear resistance has limited the application. In this work, high-performance WC reinforced MS300 composites were fabricated by high-pressure cold spray, which enables the additive manufacturing of bulk material well below its melting point. XRD analysis shows that no phase transformation occurred either to the WC reinforcements or the MS300 matrix. The distribution and morphology of the WC particles in the composite samples were characterized by X-ray computed tomography (XCT). The results show that a high retainability (85.4%) of WC particles was obtained at high working parameters (N_2, 5 MPa, 900 °C), and the solution-aging treatment resulted in decreased WC volume fraction and smoothing of WC shape. Microstructure observation of WC evolution shows that a thick diffusion layer was formed around the WC particle after solution-aging treatment significantly improving the interfacial bonding. Due to the more severe plastic deformation and higher WC retainability, the as-fabricated samples with higher propelling gas pressure demonstrate a higher tensile strength and better wear resistance. It is found that a higher solution temperature (1000 °C) can lead to an enhanced cohesive bonding within the composite. Finally, the solution-aged composite shows an excellent wear resistance under the improved WC bonding and precipitation hardening.

Keywords: Cold spray; WC; Maraging steel; X-ray Computed Tomography; EBSD; Tribological performance

*Corresponding author: Xingchen YAN, xingchen.yan@utbm.fr, Yingchun XIE, yingchun.xie@hotmail.com, Jiang WAG, jiangwang@i.shu.edu.cn

1. Introduction

Maraging steel 300 (MS300) is an iron–nickel alloy with absence of carbon, which uses elements such as molybdenum, cobalt, titanium and aluminum as substitutes to produce precipitation-hardening in iron-nickel martensite [1, 2]. Based on the precipitation of intermetallic compounds, the maraging steel 300 presents outstanding properties such as good mechanical strength, toughness, weldability and resistance to crack propagation. It has been widely applied in the fields like automotive, aircraft and aerospace, and tool and die industries, such as rocket motor casings and landing gears, conformal cooling channels, shafts, and fasteners. Upon the treatment procedures of solution and aging, outstanding mechanical properties and stable microstructure can be achieved on MS300 through the formation of lath martensite with high dislocation, solution strengthening of alloy elements and precipitation strengthening by intermetallic compounds [3, 4]. Nevertheless, with the development of industry technology, it brings forward an increasing demand of comprehensive performance for maraging steel 300, especially the high tribological performances of MS300, which can extend its applications [5].

WC-reinforced metal matrix composites (MMCs), combined metallic properties with ceramic, have been fabricated by different manufacturing methods and widely investigated in recent years [6-8]. For example, the powder-bed based AM technologies via laser or electron beam have been proposed for the fabrication of WC-based MMCs [9-11]. It is also reported that the WC-reinforced MMCs are fabricated by using conventionally high temperature processes such as high velocity oxy-fuel (HVOF) [12, 13] and laser cladding [14, 15], where the high cohesive strength is achieved by partial or complete melting of feedstock particles. However, the serious oxidation, phase change and even decarburization of carbide phase cannot be avoided in these high-temperature fabrication methods, which may result in the deterioration of mechanical properties.

To eliminate the degradation of MMCs properties under high processing temperature, the newly emerging cold spray (CS) (or known as cold gas dynamics spray, kinetic spray) [16, 17] has attracted increasing attentions as a solid-state deposition technology. Prior to the impact onto substrate, the micro-sized feedstock particles are accelerated to high velocity (300-1200 m/s) by a supersonic gas flow (air, nitrogen or helium) through a de-Laval nozzle [18]. Owing to the low temperature of the propelling gas below its melting point (about 300 to 1000 °C) and short interaction time, the deposited particles can well maintain the solid state [19-21]. The high-velocity impact of metallic particle onto substrate can result in serious plastic deformation within several tens of nanoseconds. Similar with explosive welding, the breaking and extrusion of original oxide-film on feedstock particle can promote the high-quality metallurgical bonding within CS sample [20, 22]. As a result, the CS technology enables the retainability of its original chemical composition and properties in feedstock, and effectively minimize the serious oxidation, phase change and thermal stresses in high-temperature processing [23, 24]. For the moment, the CS technology has been successfully applied in the fabrication of temperature-sensitive materials like aluminum [25, 26] and copper [17], high performance alloys like Ti6Al4V [27, 28] and Inconel [29, 30] as well as various MMCs with different reinforcements [8]. By accounting the high production rate and no

limitation of fabrication size, CS has been recognized as an effective method for additive manufacturing [31, 32] and dimensional damage repair [25, 33].

In the same manner, the unique “cold” feature of CS technology can effective protect the WC particles in MMCs material from oxidation and decarburization. Recently, the WC reinforced MMCs have been frequently reported fabricated by CS. Lioma et al. [34] fabricated WC-Ni coatings by using a low-pressure CS system with mechanical mixed powders and sintered agglomerated powders. However, only 11-29% of WC particles were retained in the as-sprayed coatings. Similarly, Melendez et al. studied [35] the microstructure evolution and coating properties of WC reinforced MMCs with Ni as binder phase. Alidokht et al. [36] reported that the wear resistance of Ni coating fabricated by high pressure CS system can be significantly improved through the reinforcement of 36.2 vol% WC particles, but with a low WC retainability of 29.0%. Besides, efforts were also made to fabricate the WC-Co coating [37, 38] by CS within the past decades. The extremely high deposition parameters were used to promote metallic bonding by inducing sufficient plastic deformation of feedstocks. It can be concluded that the above-mentioned works have a typical low retainability of WC in as-sprayed coating compared with the feedstock. Furthermore, the low processing parameters cannot obtain sufficient mechanical property and microhardness to realize their industrial application.

Therefore, this work aims to use high-pressure CS system to manufacture high-performance WC reinforced maraging steel 300 (MS300) composites. To the author’s knowledge, few studies [11] have been made on the fabrication of high-performance MS300 by CS. The solution-aging treatments were conducted to promote the inter-particle diffusion, stress releasing and precipitation strengthening and hardening. A systematic study was carried out focusing on the microstructure characterization and mechanical properties. The X-ray computed tomography was applied to investigate the distribution and morphology of WC particles within the CS WC/MS300 composites. The EBSD and SEM observation were used to study the microstructural evolution. At last, the tribological and tensile properties of CS WC/MS300 composites were studied.

2. Experimental details

2.1. Sample preparation and heat treatment procedure

In this work, the spherical maraging steel 300-grade powder (EOS GmbH, Germany) was used as the matrix material for the composite. Based on the literature study [39, 40], the irregular WC powder (Golden egret, Xiamen, China) with a size range of 1-6 μm was used as the reinforcement particles to maximize the deposition efficiency in CS. The mixture of 85% MS300 and 15% WC powders in weight percentage were mechanically blended in a in a tumbling mixer during 200 mins before fabrication, which corresponds to a volume fraction of 91.7%/8.3%. The surface morphology of the powder mixture is shown in Fig. 1 (a). The EDS surface mapping in Fig. 2 (b) indicates the distribution of spherical MS300 powders and irregular WC powders. The magnified view in Fig. 1 (c) show the WC morphologies featured by slight aggregation. The cross-sectional morphologies were shown in the etched and EBSD images of MS300 powder in Fig. 1 (c)

and (d), respectively. The MS300 powders exhibit an equiaxed grain structure with an average size of 150.1±180.3 nm as a result of the rapid solidification during gas-atomization process. The size distribution of the MS300 and WC particles are given in Fig. 1 (f).

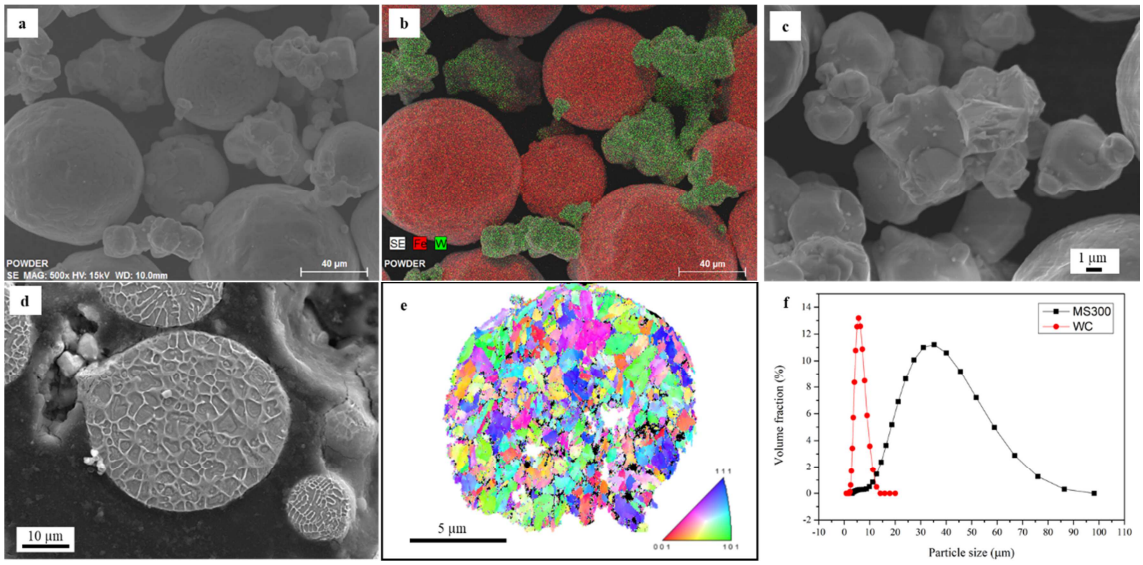

Fig. 1 SEM morphologies: (a) mixed feedstock powders, (b) EDS mapping showing each item (MS300 in red and WC in green), (c) magnified view showing the WC particles, (d) cross-section of etched MS300 powder, (e) Inverse polar figure (IPF) + IQ by EBSD showing the grain structure and (f) the size distribution of MS300 and WC particles.

The WC/MS300 composite coating was fabricated with a PCS-1000 CS system (Plasma Giken Co., Ltd., Japan), whereas the schematic sketch is given in Fig. 2 (a). Nitrogen was used as powder carrier gas and propelling gas for the premixed MS300 and WC powders. Two sets of fabrication parameters including different pressures of propelling gas were used: (1) 900 ºC and 4.0 MPa referred as AF1, (2) 900 ºC and 5.0 MPa as AF2. The standoff distance from the nozzle exit to the substrate surface was 30 mm. The hatch distance between successive passes was 2 mm. In addition, the nozzle traverse speed was 100 mm/s. Thick composite coatings were fabricated on grit-blasted 304 stainless steel substrates. Based on ASTM E8/E8M standard [41], the tensile samples were machined from the in-plane surface of as-fabricated part following substrate removal, whose dimensions are given in Fig. 2 (b). Despite the anisotropic feature of CS coatings, the in-plane samples were chosen due to its generally higher strength than that of out-plane [32].

To further improve the mechanical properties of CS composite coating, the heat treatment procedures including solution and following aging were conducted on the as-fabricated samples. Two heat treatment procedures include: (1) solution at 800 ºC for 1 h and aging at 480 ºC for 6 h referred as HT1 and (2) 1000 ºC for 1 h and aging at 480 ºC for 6 h referred as HT2. All the heat treatments were conducted in a home-made tube furnace with an argon protective atmosphere to avoid oxidation and followed by air-cooling.

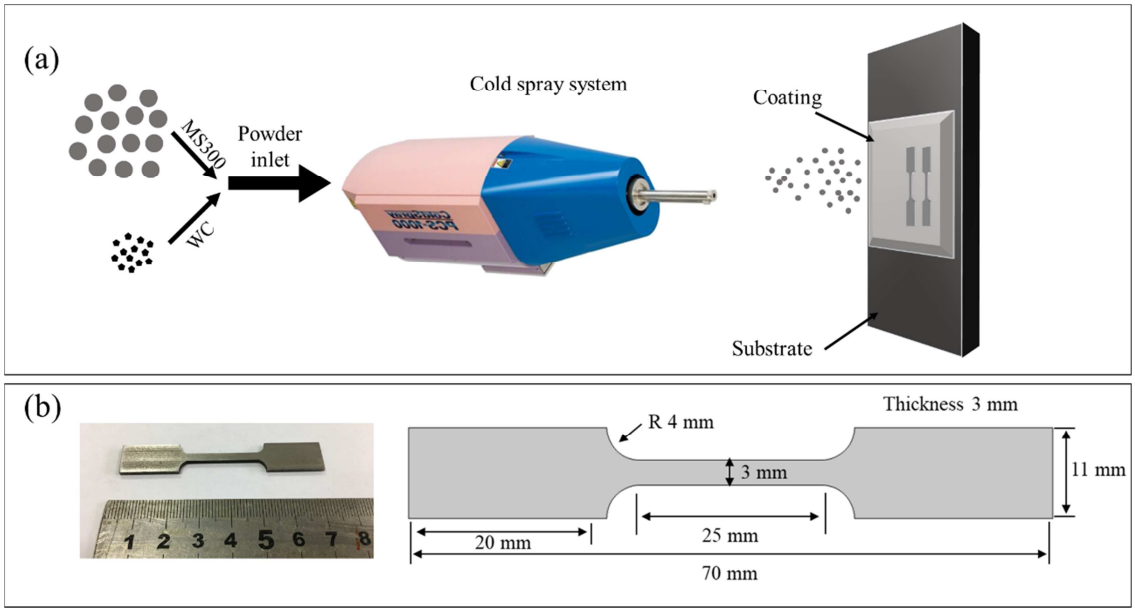

Fig. 2 (a) Schematic sketch of the CS fabrication process and (b) digital photo (left) and dimensions (right) of the tensile sample.

2.2. Material characterization

The coating microstructure was firstly observed by an optical microscopy (OM). To reveal the morphology evolution and particle deformation, the polished samples were etched at room temperature for 20 s by a solution of 25 ml HNO_3, 50 ml HCl, 1 g $CuCl_2$ and 100 ml distilled water. The microstructure was then observed by scanning electron microscopy (SEM), with a device equipped with an energy-dispersive spectroscopy (EDS) unit (JSM 5800 LV, JEOL, Japan). Texture and crystallographic orientations were characterized by a SEM (Nova NanoSEM 450) equipped with electron backscatter diffraction (EBSD). EBSD characterization is carried out under an acceleration voltage of 20 kV, a step size of 60 nm and spot size of 6 μm. The spatial and angular resolutions of the EBSD system are 50 nm and 0.5°, respectively. Phase composition was tested by X-ray diffraction (D800, Siemens, Germany) using a Cobalt anticathode (k = 1.78897 Å) operated at 35 kV and 40 mA.

Generally, the image processing via the optical microscope observation is used to investigate the content and morphology of the reinforcement particle and pore within an MMC sample fabricated via AM methods like CS and Selective laser melting (SLM). However, the 2-dimensional observation cannot provide the exact particle distribution and content within the MMC bulk [42]. In this work, an X-ray computer tomography (CT) (X5000, North Star Imaging, USA) is used to obtain the pores and reinforced WC particles in CS-fabricated composite sample. As shown in Fig. 3, cubic samples with dimensions of 3×3×5 mm^3 were placed on the 360° rotating stage of the X-ray tomography and analyzed at an acceleration voltage of 100 keV and a current of 90 μA. A volume of 1000×1000×1000 μm^3 was studied with a precision of 4 μm/voxel. As can be seen on the right side of Fig. 3, the three-dimensional volume

was then reconstructed using the Amira-Avizo software (FEI Visualization Sciences Group, Software, Germany) and the porosity and WC content can be computed based on the volume ratio to the bulk cube.

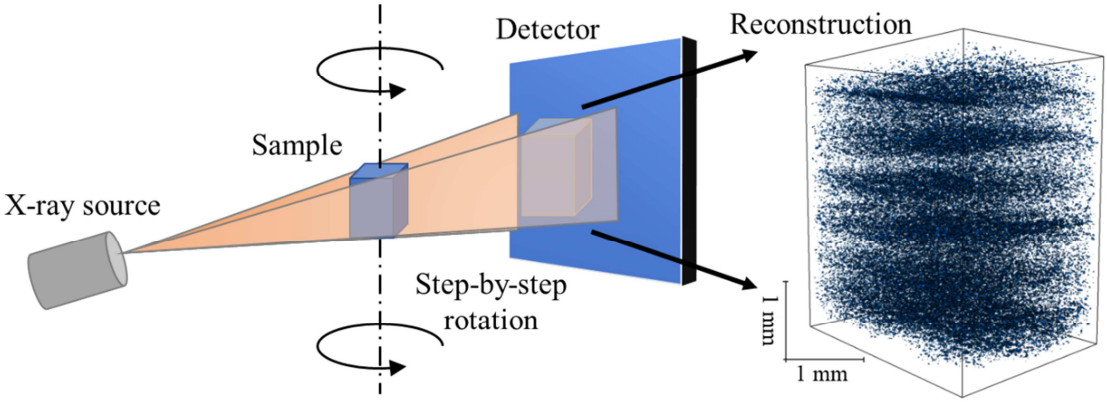

Fig. 3 Schematic sketch of measurement of WC particles within WC/MS300 composite via the X-ray Computed Tomography.

2.3. Mechanical property

Room-temperature tensile tests were performed according to the ASTM E 8M standard at a strain rate of 1 mm/min. The ultimate tensile strength (UTS), elongation at fracture and elastic modulus were obtained from a universal testing system (INSTRON 5982, USA). Strain-to-failure was recorded by strain gages and extensometers with a 10 mm range. The extensometer was attached to the gage section of the test specimen and removed after the yielding stage to keep the accuracy. The Vickers hardness was measured at the cross-section using a microhardness tester (Leiz-Wetzlar, Germany) at a load of 0.2 kg and an indentation time of 25 s, where the result is the average of 15 measurements.

Dry sliding wear tests were conducted at ambient temperature with a tribometer implement (CSEM, Switzerland). Before the tests, the roughness Ra of the sample was kept less than 0.15 μm to rule out its influence wear performance. The counterpart material was an Al_2O_3 with 6 mm diameter, which was grinded and polished using sandpaper and cleaned with ethanol before the tests. The friction test load was 0.5 kg, with a rotational speed corresponding to 0.100 m/s for 200 m with the radius of 3 mm. The coefficient of friction (COF) was recorded during sliding. After friction test, the surface of worn samples was observed by SEM and then analyzed by EDS. The cross-sections of the worn tracks were measured by a profilometer (Altisurf 500, France). The worn volumes of the samples were calculated via the product of the cross-sectional areas by the length of worn tracks.

3. Results and discussion

3.1. Phase composition

In the conventional thermal spray or high-temperature AM processes, the unfavorable decarburization, decomposition or even phase transformation can affect the microstructure and mechanical properties of WC-based composites. As shown in Fig. 4, the XRD spectra demonstrate that the phases of martensite and

WC are well retained within the AF composite samples by comparing with feedstock powder. It exhibits the unique advantage of CS technique with low processing temperature in preventing phase transformation and retaining original crystal structure of the raw material, which can help improve the mechanical properties of WC reinforced MS300 composite [32]. Besides, it should also be noted that the peak intensity of WC phase is weakened in AF sample than that of powder, which can be attributed to the WC loss during deposition. Besides, a rightward peak shift of martensitic phase can be observed through the comparison between initial powder and AF samples. It can be understood as the grain refinement and micro-straining during the severe plastic deformation of CS particle with high-velocity, which will be discussed through the EBSD analysis in the following section. After the solution-aging treatment, the phases of martensite and WC were well retained in the HT samples. At the same time, the residual γ-peak indicating the austenite phase is weakened after the conducted HT procedures. Generally, the complete martensite transformation will produce an austenite-free matrix after the solution treatment. However, it is widely accepted that the austenite reversion cannot be avoided during the aging treatment as a result of Ni_3Ti decomposition [43].

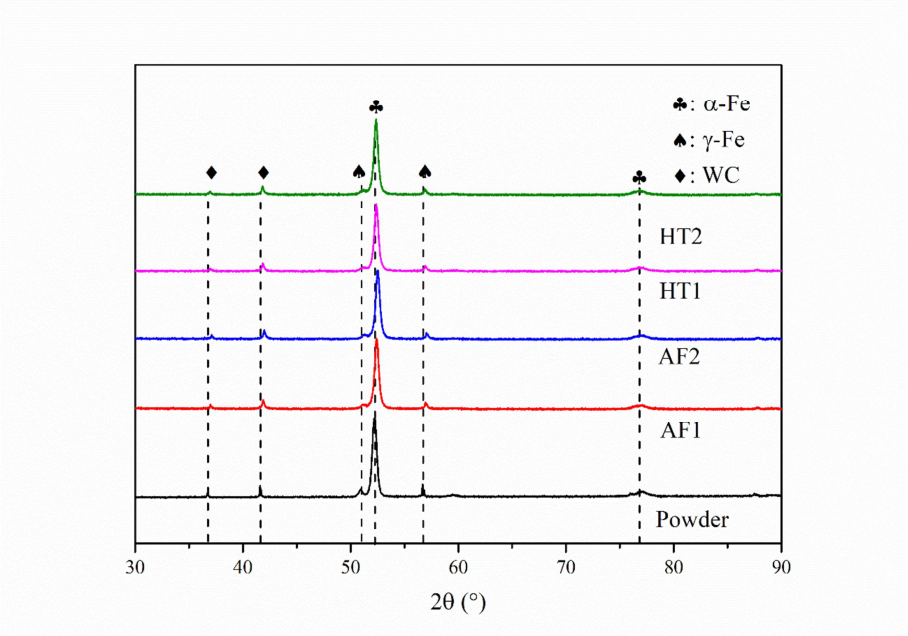

Fig. 4 XRD spectra of the feedstock powder and WC/MS300 composites at different conditions.

3.2. WC reinforcement particles via XCT

The distributions of WC reinforcement particles within the WC/MS300 composite samples at different conditions are illustrated in Fig. 5. The WC particles through the reconstruction after XCT measurement are colored according to the distribution of equivalent diameter, which is the corresponding spherical diameter of the object with equal voxel volume. The volumetric contents of WC particles within the composite samples are evaluated and given in Fig. 6 (a). The equivalent diameters of WC particles are then

analyzed to understand the evolution of reinforcement particles at different conditions, which is given in Fig. 6 (b). The term of equivalent diameter can be used to evaluate the effective size of the WC particles with the irregular shapes [42, 44]. From Fig. 6 (a), it can be seen that the high retainability of the WC particles has been achieved in the cases of as-fabricated sample by using the high-pressure CS system with high-end deposition parameters. By improving the propelling gas pressure from 4.0 MPa to 5.0 MPa, the retainability of WC particle was further increased from 78.8% in AF1 to 85.4% in AF2, which can be also observed from the reconstruction images in Fig. 5. The equivalent diameter of WC particle and the corresponding quantity is illustrated in Fig. 6 (b). A majority of the observed WC particles exhibit the equivalent diameter less than 20 µm, which corresponds well with the size distribution of starting materials. However, the WC particle with equivalent diameter around 40 µm can also be found in the XCT reconstruction image. Such phenomena can be understood as the accumulation and agglomeration of WC particles during the CS deposition process. A typical 3-dimensional morphology of the WC agglomeration obtained by the graphical reconstruction after XCT is given in Fig. 7 (a). It demonstrates the agglomeration of connecting WC particles uniformly distributed around the extensively deformed MS300 particle, which will be discussed in detail in the following section. Such phenomena of reinforcement particles in the fabrication of CS MMCs is frequently reported [35, 38].

As shown in Fig. 5 and Fig. 6 (a), the WC content is significantly decreased after the solution-aging treatment. It can be explained as the partial diffusion during the high temperature solution process. As a result, the decrease of WC content is more evident in the case of HT2 sample with solution temperature of 1000 °C than that of HT1 (800 °C). As it can be observed in Fig. 5 (c) and (d), both the particle size and density of WC particle are decreasing after solution-aging treatment. As illustrated in Fig. 6 (b), both the equivalent diameter and its corresponding counts experienced an evident decrease after solution-aging treatment. The particle aggregation with large equivalent diameter has been reduced due to the partial diffusion during high-temperature solution treatment. As shown in Fig. 7 (b) and (c), the WC particle within the WC/MS300 composite samples exhibit nearly spherical shapes after high-temperature solution treatment. The detailed morphology evolution of WC particle after HT will be discussed with the cross-sectional observation through SEM.

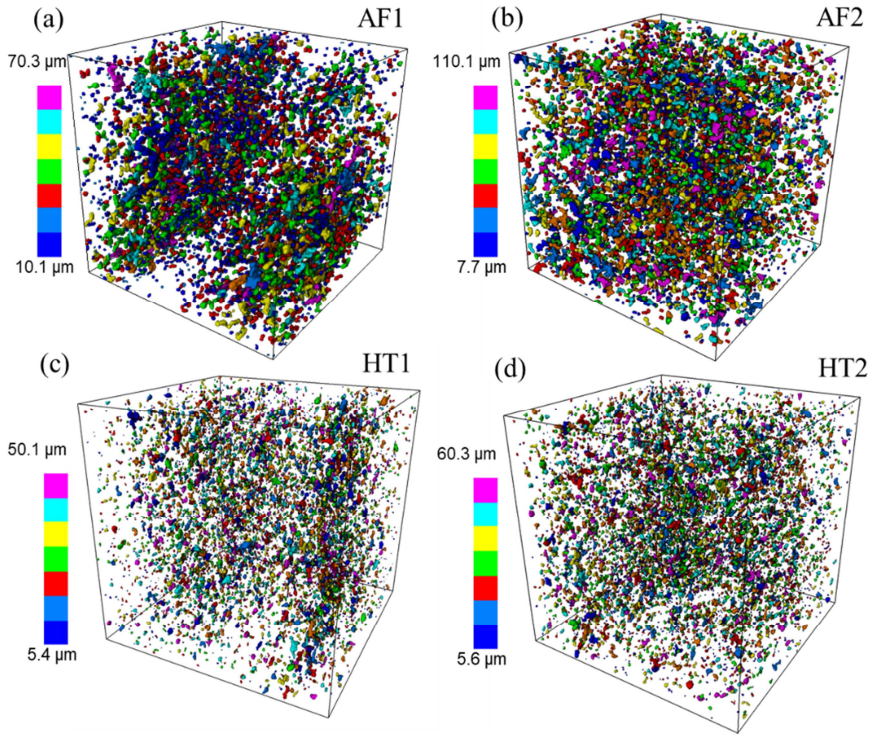

Fig. 5 Distribution of WC particles within the WC/MS300 composite samples (1×1×1 mm^3) fabricated by CS in different conditions with color indicating the equivalent diameter.

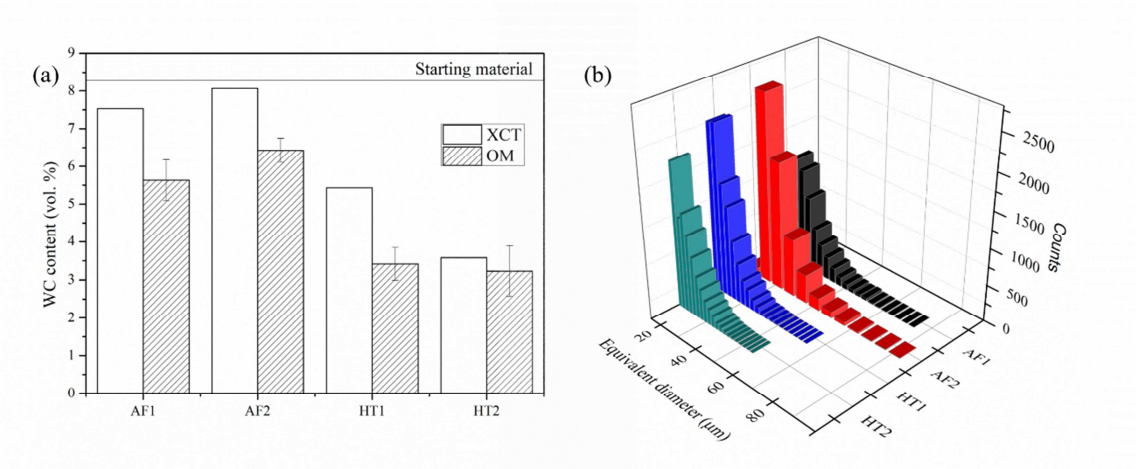

Fig. 6 Variation of the (a) volumetric contents and (b) equivalent diameter of WC particles in WC/MS300 composite samples obtained via XCT.

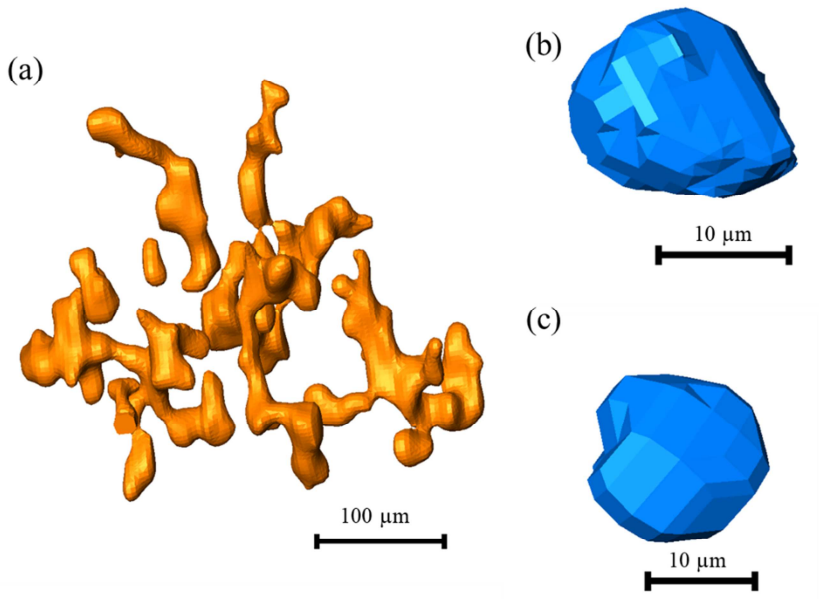

Fig. 7 Typical morphologies of the remaining WC particles within the WC/MS300 composite samples: (a) agglomeration of WC particles in as-fabricated sample, and partial-melted WC particle in HT1 (b) and HT2 (c) samples.

3.3. Microstructure evolution

Fig. 8 shows the OM images of cross section and surface of the WC/MS300 composite samples at conditions of AF and HT. The AF samples fabricated by CS show a highly densified morphology with few defects of pores or cracks. It can be attributed to the extensive plastic deformation of MS300 particle under the successive deposition of subsequent MS300 particle and in-situ peening of reinforcing WC particles. According to the XCT measurement, the composite samples at AF and HT conditions all exhibit the porosity lower than 0.3%. Meanwhile, the uniform distribution of the reinforcement WC particles within the MS300 matrix. As indicated in Fig. 8, the localized agglomeration of WC particles can be seen from the cross-sectional and surface images, which corresponds well with the XCT reconstruction images.

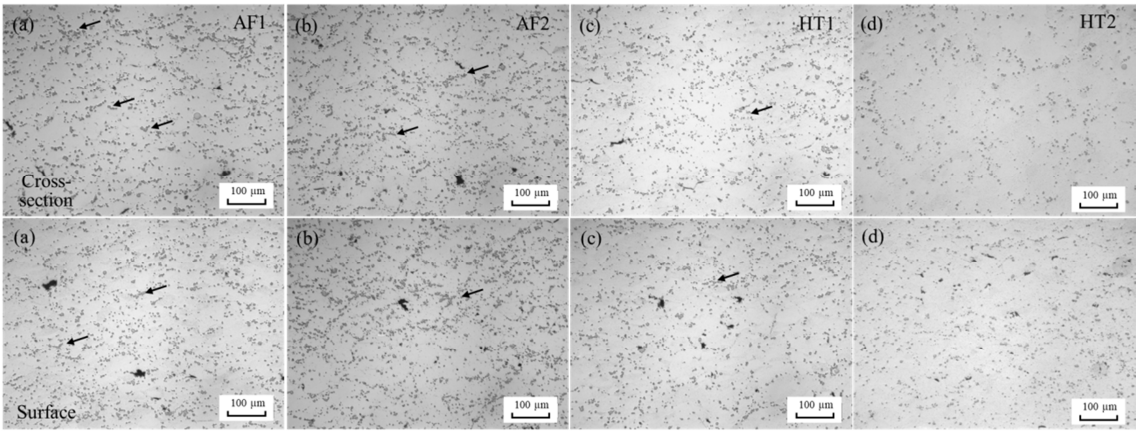

Fig. 8 OM morphologies of the cross-section (first row) and surface (second row) of the WC/MS300 composite samples at different conditions.

To reveal the particle boundary and its deformation behavior, Fig. 9 is given to show the etched cross-sectional morphologies and the corresponding magnified views of the WC/MS300 composites at different conditions. In the overviews of AF samples (see Fig. 9 (a) and (c)), the WC particles can be found uniformly dispersed surrounding the severely deformed MS300 particles. According to the magnified views in Fig. 9 (b), the equiaxed grain structure was well retained in the AF1 sample from the original powders (see Fig. 1 (b)). Meanwhile, it is evident that the grains within the deformed MS300 particles experienced elongation and deformation in the AF1 sample. As the increase of propelling gas pressure to 5.0 MPa in AF2 sample, the MS300 particles were experienced more intensive plastic deformation owing to the increased impact velocity, and the obvious material jet and resulting intertwining were formed as the marked white arrows. It can also suggest a better inter-particle bonding through the strong mechanical interlocking and the further formation of metallurgical bonding. Besides, the magnified views show the intimate bonding between the deposited WC particles and deformed MS300 matrix, without obvious cracks, which can benefit the improved mechanical properties of the CS composites.

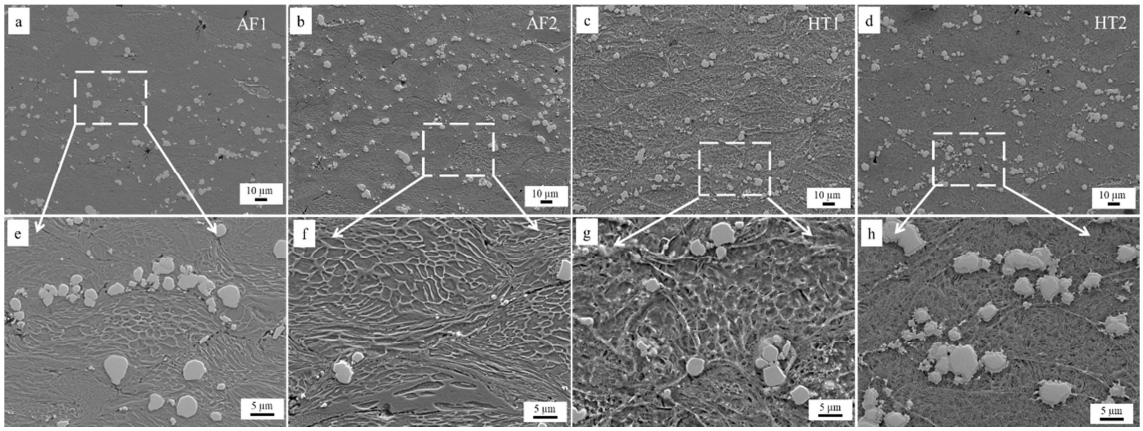

Fig. 9 SEM morphologies of the WC/MS300 composites at different conditions, and the magnified views of the boxed areas are given in the second row.

As for the samples processed by solution and aging treatments, the HT1 and HT2 demonstrate distinct morphologies compared with the AF ones. As the overview of HT1 is given in Fig. 9 (e), the interfaces between the deformed particles were blurred and partially disappeared due to the high-temperature solution annealing treatment. Due to the highly densified microstructure and intimate bonding in AF samples, the following solution and aging treatment can effectively promote the interfacial diffusion between MS300 particles and the reinforced WC particles. By further improving the solution temperature to 1000 ºC, the interfaces between the deformed MS300 particles were eliminated (see Fig. 9 (g)).

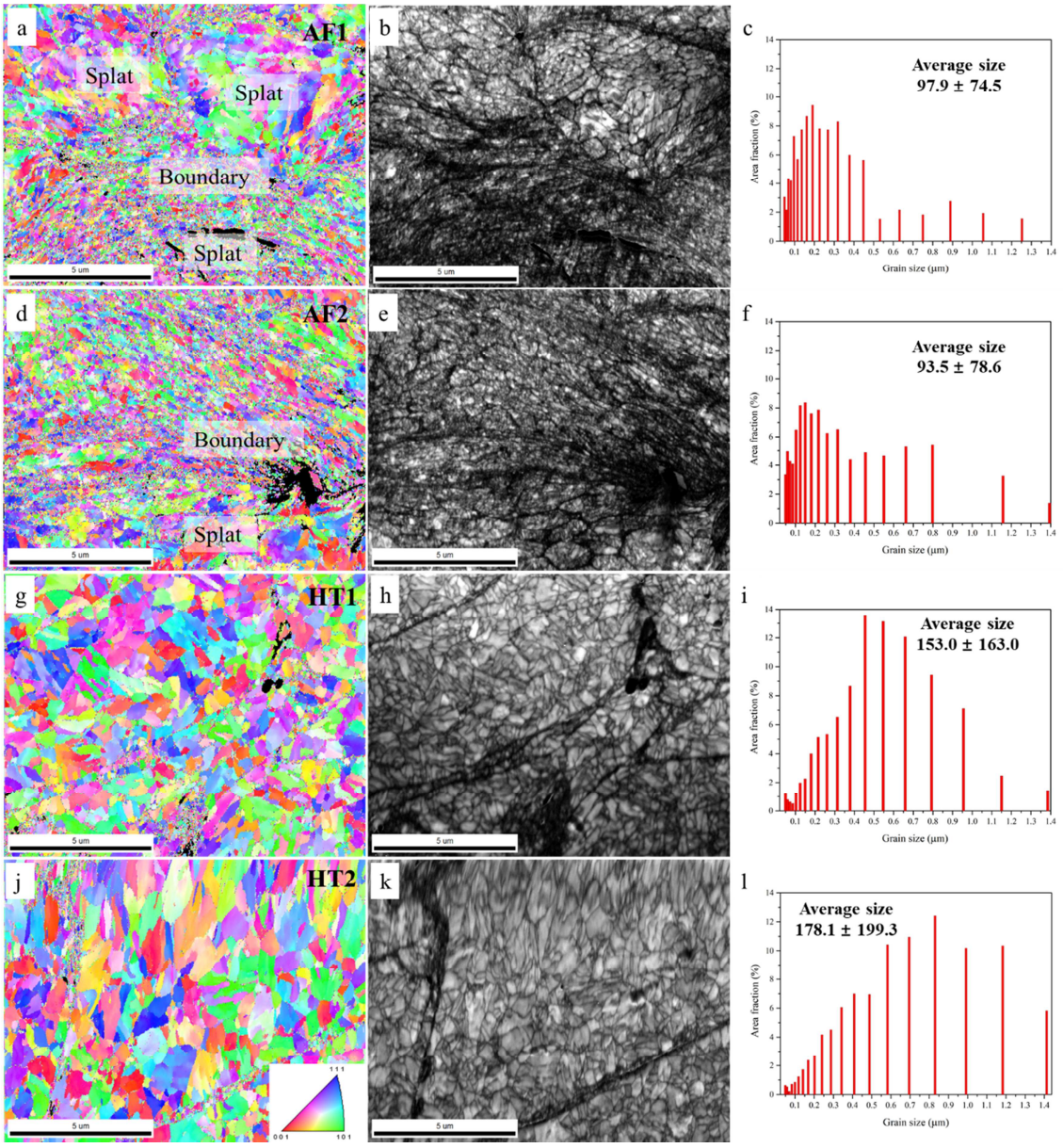

Fig. 10 EBSD characterization of the MS300 matrix in the composites at different conditions: first row column is Inverse pole figure (IPF) maps, second one is pattern quality maps, third one is grain size distribution. (a-c): AF1, (e-f): AF2, (g-i): HT1, (j-l): HT2.

To further understand the microstructure evolution, EBSD characterization was conducted on the MS300 matrix region with a dimension of 13×10 μm composed by two or three deformed particles in composite. As the IPF maps are shown in the Fig. 10 (a) and (d), the AF1 and AF2 samples demonstrate the typical anisotropy of the grain orientation and deformation, which is frequently reported in a CS-fabricated microstructures [45, 46]. As indicated in Fig. 10 (a) and (b), it is obvious that the original equiaxed grains were well remained within the deformed splat. Meanwhile, a large quantity of ultrafine grains between the range of 50 to 100 nm were generated at the inter-particle boundaries, which shows similar morphologies with the SEM observation in Fig. 9. It can be attributed to the dynamic recrystallization due to lattice and subgrain rotation [47]. With the increase of propelling gas pressure to 5 MPa (see Fig. 10 (d)), the grain refinement at the boundary area becomes more prominent, which exhibits a smaller average grain size (93.5 ± 78.6 nm) than that of AF1 (97.9 ± 74.5 nm). Such grain refinement can be attributed to increased plastic deformation caused by two main facts, which are the higher particle velocity prior to impact and the enhanced peening effect by WC particle [48]. As for the HT samples, the IPF maps in Fig. 10 (g) and (j) demonstrate an evident grain growth compared with the AF. The high-temperature solution for 1 h can significantly promote the static recrystallization [49] in the AF samples, which can result in the observed grain growth. Such grain growth is more prominent in HT2 sample at a higher solution temperature of 1000 °C than that of HT1. Meanwhile, it is seen that the inter-particle boundaries between deformed MS300 particle were disappeared after the solution-aging treatment. The ultrafine grains originally located at boundary areas were replaced by the equiaxed grains after the HT. Fig. 10 (h) and (k) show the improved pattern quality of the HT samples than those of AF (see Fig. 10 (b) and (e)), due to the reduced dislocation density caused by static recrystallization at the particle boundary areas.

To better understand the role of reinforcement particles, the evolution of WC particles at different conditions are observed by magnified SEM image and EDX scanning. As for the as-fabricated sample, the WC particle was embedded in the MS300 matrix, and the particle interface can be clearly identified from the deformed MS300 particle. From Fig. 11 (a), the intimate bonding was formed between the reinforcement WC particle with no interfacial cracks or pores. Different from the laser-based AM methods [9], the WC particle experienced no melting or decomposition during the CS deposition. Meanwhile, the successive impact of WC particles during deposition can lead to a strong in-situ peening effect, which can significantly improve the work-hardening and resultant plastic deformation of the MS300 matrix. As shown in Fig. 11 (a), the kinetic energy of the reinforcement WC leads to the severe plastic deformation of the surrounding MS300 grains. As for the cases of HT samples in Fig. 11 (b) and (c), an increasingly prominent diffusion layer can be seen formed between WC and MS300 matrix with the increasing solution annealing temperature. According to the EDX scanning along the particle interface, a diffusion layer can be clearly observed surrounding the WC particle. It can be seen that such diffusion layer is composed by a mixture of W from reinforcement particle and Fe, Ti, Ni and Co from matrix. Such metallurgical bonding resulting from atomic diffusion can enable the formation of a series of carbide compounds and further improvement of the bonding strength between reinforcement and matrix in the CS composite.

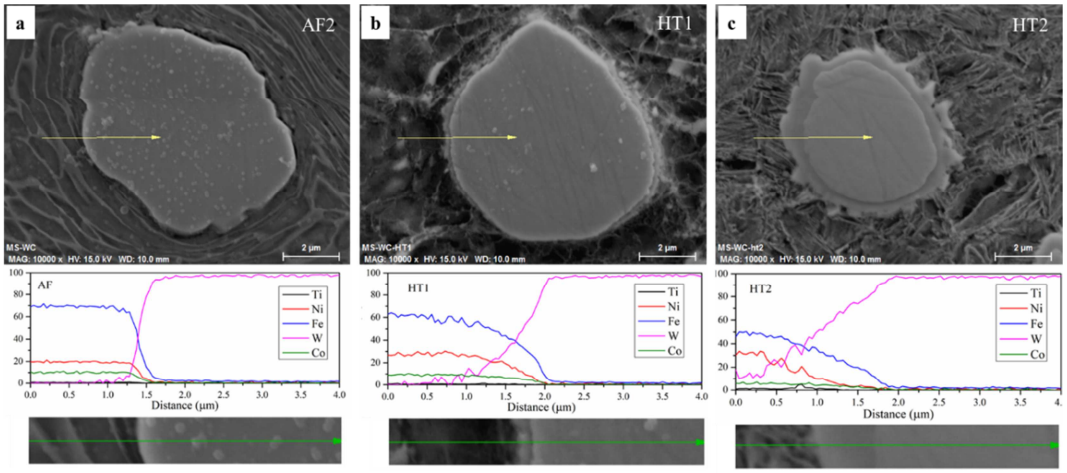

Fig. 11 Gradient interface between WC particle and MS300 matrix at different conditions and element contents along the indicated line by EDX: (a) AF2, (b) HT1, (c) HT2.

Fig. 12 gives the magnified view of the diffusion layer formed at different solution annealing temperatures. With the increasing HT temperature, the thickness of the diffusion layer was increased from 0.28 to 0.68 μm. As shown in the EDX result in Fig. 11, the diffusion layer was formed due to the partial melting and decomposition of WC particle during HT. At a higher HT temperature, a thicker diffusion layer was formed around the WC particle with more evenly distributed element mixture.

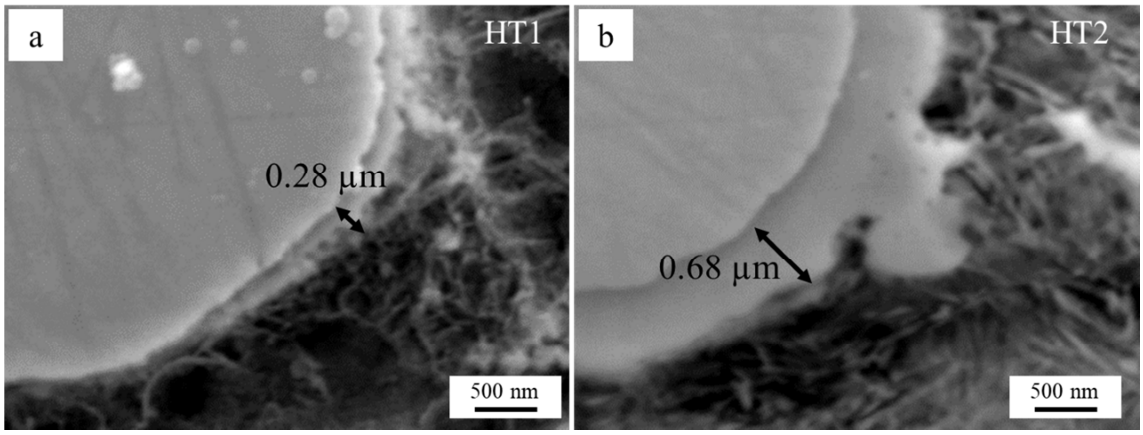

Fig. 12 Magnified view of the diffusion layer formed at different solution annealing temperatures: (a) HT1 and (b) HT2.

3.4. Microhardness

In this work, the WC particle was used as reinforcement to improve the mechanical properties of the MS300 via CS process, and solution-aging treatment was then conducted to achieve the further improvements. Fig. 13 shows the evolution of WC reinforced MS300 composite at different conditions. At the as-fabricated conditions, the AF2 sample with higher propelling gas pressure of 5.0 MPa possesses a higher microhardness than that of AF1. According to abovementioned microstructure analysis, the lower

porosity value (see Fig. 8) and finer grain size (see Fig. 10) as a result of severer particle deformation can be considered as the main reasons contributing to the higher microhardness value of AF2 sample. It is obvious that the increased microhardness is achieved after the solution and aging-hardening treatment in HT1 and HT2 samples. Such significant hardness improvement can be attributed to the precipitation of Ni_3(Ti, Al, Mo) within the martensite matrix during aging hardening at 480 °C for 6 h. Meanwhile, the diffusion of W element into matrix and formation of carbide compound can also contribute to the hardness improvement in the HT samples. However, the HT2 sample with a higher solution temperature of 1000 °C exhibits a lowered microhardness value than that of HT1. The reduction of microhardness is mainly due to the coarsened grain size at a higher solution-annealing temperature, which contributes to the offset of precipitation hardening in aging treatment.

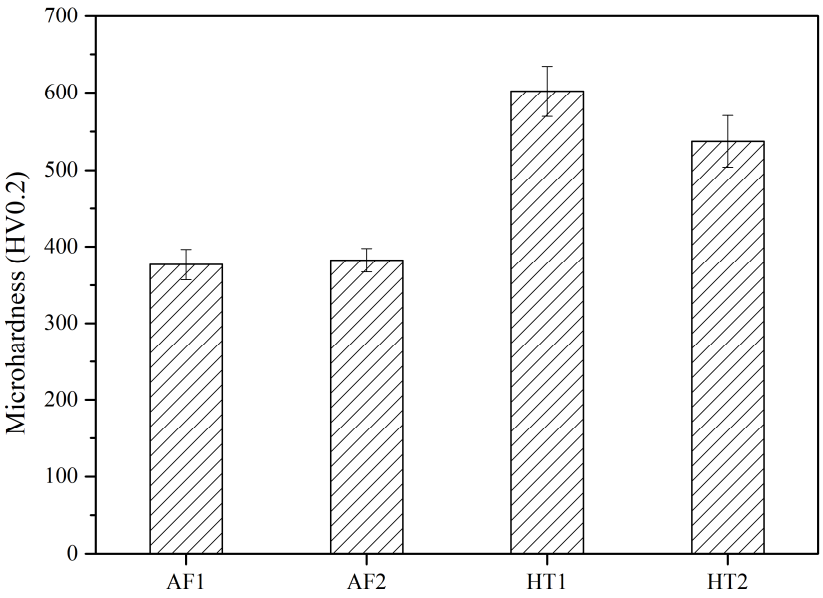

Fig. 13 Microhardness comparison of WC/MS300 composites at AF and HT conditions.

3.5. Tribological performance

Fig. 14 shows the variation of coefficients of friction (COF) and wear rate of WC/MS300 composite sample at different conditions. As the COF curves are shown in Fig. 14 (a), all samples experienced a typical fluctuation at the early stage of friction test, while the stabilization was reached after the sliding distance of 60 m. As shown the Fig. 14 (a) and (b), both the average COF values and wear rate demonstrate the similar trend with the microhardness (see Fig. 13). AF2 sample with higher propelling gas pressure possessed a lower average COF value and lower wear rate than that of AF1. Similar with the hardness difference, the enhanced work-hardening at higher particle impact velocity lead to a better wear resistance

of AF2 sample. It can be seen that the HT samples show superior wear-resistance featured by lower wear rate and COF values than those of AF. Such low wear rate ($4.11 \pm 1.33\times10^{-6}$) can be comparable with the reported WC-Co-Ni coating ($3.382 \pm 1.020\times10^{-6}$) with WC content more than 60 % [38]. Such improved tribological performance at HT condition is mainly due to the carbide diffusion layer and precipitation hardening during the solution-aging treatment. Besides, it is interesting to notice that the HT2 sample exhibits a weakened wear resistance than that of HT1 due to the lower solution treatment duration and temperature.

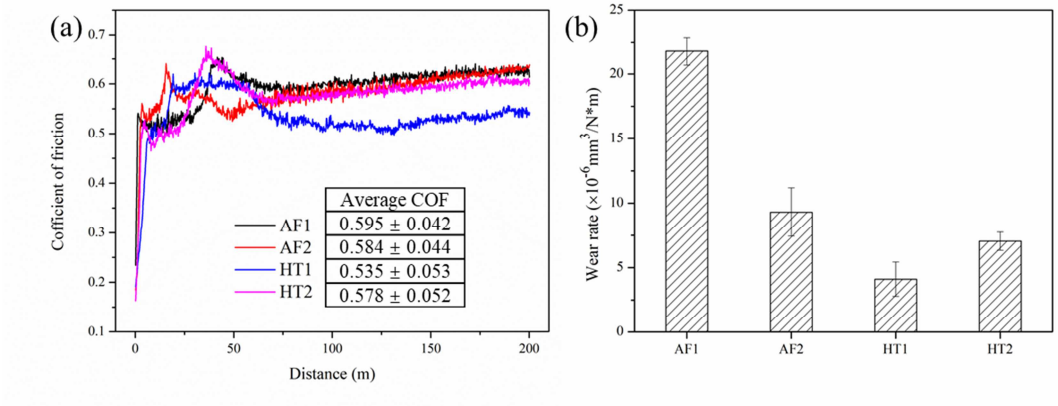

Fig. 14 Tribological performance of WC/MS300 composites at AF and HT conditions: (a) COF variation and (b) wear rate.

The worn morphologies of different WC/MS300 composites after wear test were given in Fig. 15 to better understand the wear mechanism. As for the AF and HT samples, the worn morphologies are mainly characterized by the disconnected tribolayer and evident wear scars, indicating the adhesive wear mechanism. Through the mechanical mixing and smearing of wear debris during sliding, the observed tribolayer will be formed on sample surface, which leads to the stabilization of COF curve after the initial fluctuation stage in Fig. 14 (a). As the EDS mapping on the magnified area is given in Fig. 16, the tribolayers formed in the AF2 and HT1 samples are characterized by the oxidation and the mixing elements from matrix and reinforcement particles. In addition, serious peeling-off and microcracks were formed on the tribolayer of AF samples (see Fig. 15 (a) and (b). Under the successive loading of the counterpart, the work-hardening and stress concentration can cause the generation and propagation of cracks on the tribolayer. As for the HT samples, partial tribolayer was formed on the worn surface with the obvious grooves. Different from the AF samples, the precipitation hardening of MS300 matrix during solution-aging treatment can provide an improved wear resistance to the sliding friction. Meanwhile, the high temperature solution process can promote the observed diffusion of WC particle within the matrix, and the resultant carbide diffusion layer can further benefit the wear resistance. The ameliorated interfacial bonding between WC particles and MS300 matrix can promote the tribological performance of composite. As for

the HT2 sample, the higher solution temperature lead to a more prominent decrease of grain growth and microhardness (see Fig. 10 and Fig. 13), which can well explain its deteriorated wear resistance.

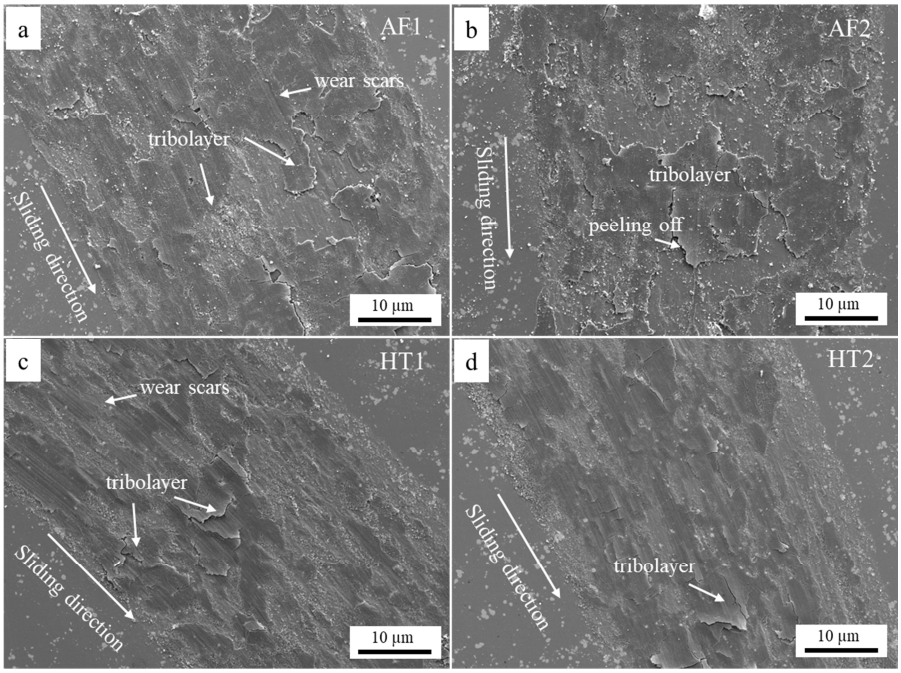

Fig. 15 Worn surface morphologies of WC/MS300 composites at AF and HT conditions.

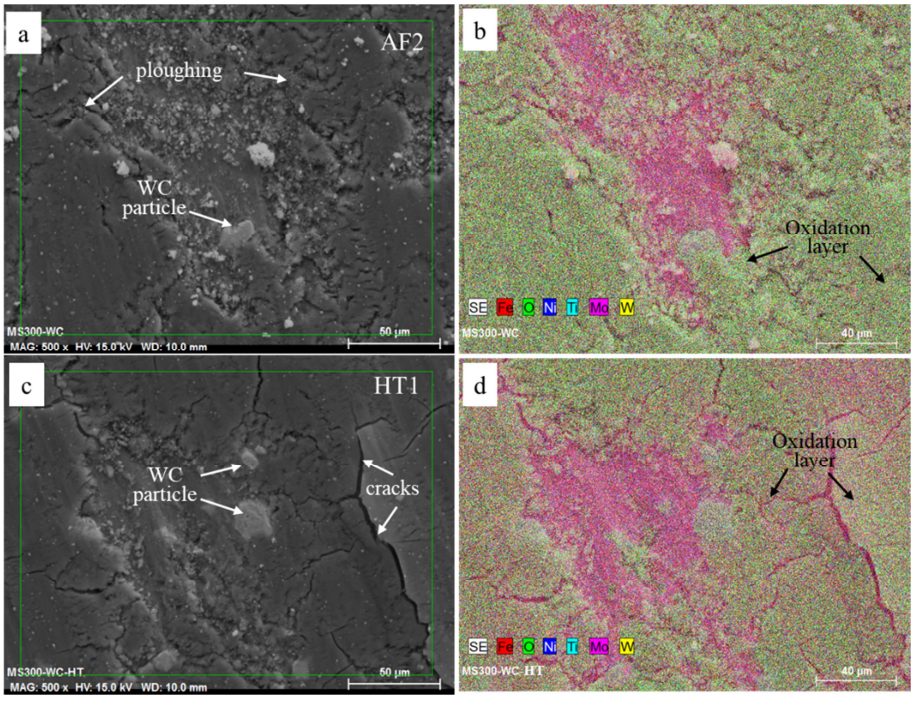

Fig. 16 Magnified view of worn morphology of WC/MS300 composites at AF2 and HT1 conditions.

3.6. Tensile performance

Fig. 17 shows the strain-stress curve of the WC reinforced MS300 composites processed at different conditions. As for the AF condition, both samples exhibit low ductility and low strength. The UTS and elongation at fracture of the AF1 sample were 147.1 MPa and 0.6%, respectively. Due to the high melting point and high hardness, the metallurgical bonding is generally limited in the AF samples [50]. The mechanical interlocking becomes the main bonding mechanism in the CS-fabricated iron-based coating [50, 51], which leads to the typical brittle feature as the tensile properties shown in Fig. 17. By increasing the propelling gas pressure to 5.0 MPa in AF2 sample, the UTS and elongation can be further improved to 308 MPa and 0.96%, respectively. It can be considered that more extensive metallurgical bonding and lower interior defects were achieved at a higher particle impact velocity in the deposition of AF2 sample. Furthermore, it should be noticed that both the AF samples exhibit limited elastic modulus values derived from Fig. 17, which are 24.9 GPa and 30.6 GPa for AF1 and AF2, respectively. The low Young's modulus and elongation values indicates the existence of porous defects in the CS WC/MS300 composite coatings [50, 52]. At the same time, the addition of reinforcing WC particles can also contribute to the low Young's modulus value than that of bulk MS300 material. Meanwhile, it is obviously that the solution-aging treatment leads to a significant improvement of both UTS and elongation compared with the AF samples, which are 744 MPa and 2.53% for HT1 and 821 MPa and 3.06% for HT2. However, the Young's modulus values were hardly improved after solution-aging treatment, which indicates the inter-particle cracks and pores were not entirely eliminated at the moderate treatment temperature. In the future work, it is considering to using the high-temperature solution-annealing treatment or hot isostatic pressing [53] to further improve the inter-particle cohesive bonding between MS300 particles and reinforcing WC particles.

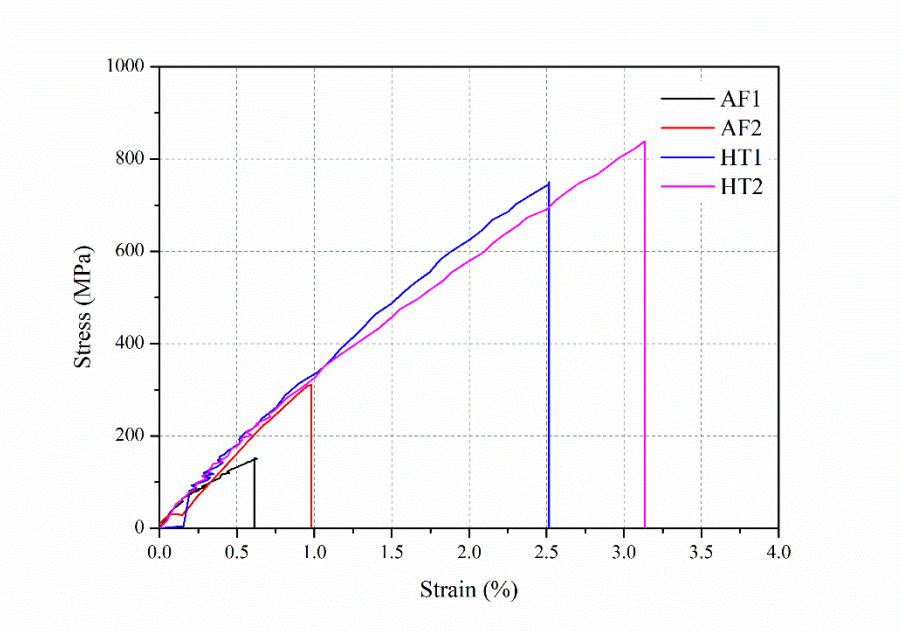

Fig. 17 Strain-stress curves of WC/MS300 composites at AF and HT conditions.

Fig. 18 shows the fracture morphologies of the AF samples after tensile test. As the overviews given in Fig. 18 (a) and (c), the fractures are mostly occurred along the interfaces between severely deformed particles in the case of the AF samples. Some interfacial cracks and pores can be found on the fracture surface, which may act as the fracture initiation during the tensile test. Such interfacial cracks and pores can also contribute to the resulting low elongation and modulus values in the AF samples. Meanwhile, the reinforcing WC particles are uniformly distributed at the inter-particle boundaries, which corresponds well with the cross-sectional morphologies (see Fig. 9). With the increase of propelling gas pressure, the increased plastic deformation of MS300 particle can be seen on the fracture surface (see Fig. 18 (c) and (d)). Such phenomena have a good agreement with the microstructure observation at cross sections in Fig. 9 and Fig. 10. As the magnified view is given in Fig. 18 (d), it is worth noticing that the extensive dimple features are formed on severely deformed particle in AF2 sample, which indicates the formation of metallurgical bonding at a higher propelling gas pressure. The increased impact velocity of MS300 particle can promote its plastic deformation. The extensive metal jet formation can benefit the fresh metal exposure and lead to the formation of metallurgical bonding [22]. Meanwhile, the increased velocity of WC particle can lead to an enhanced in-situ peening effect on the deposited MS300 particle, and the resultant cold-working can further improve the cohesive bonding within the composite [30].

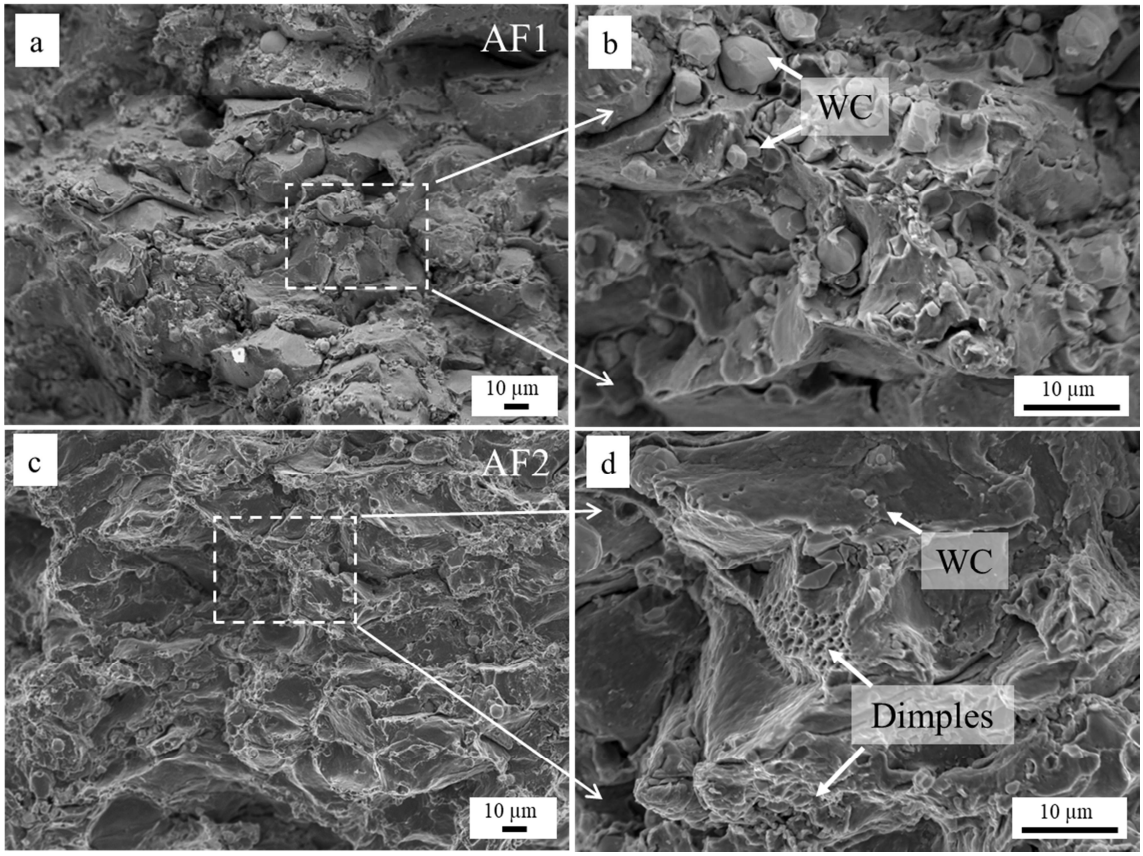

Fig. 18 Fracture surfaces of WC/MS300 composites at AF conditions at different propelling gas pressures, and the magnified views of corresponding boxed areas are given in the second column.

As shown in Fig. 19 (a), a more prominent occurrence of dimple fractures can be identified for the HT1 sample with solution temperature of 800 °C for 1 h. Meanwhile, the cleavage fractures along the deformed particles are evidently decreased, which indicates the enhanced inter-particle diffusion and blurred boundary after heat treatment. Such phenomena correspond well with the microstructural observation in Fig. 9 and Fig. 10. As the solution temperature is increased to 1000 °C, such dimple fractures are more extensive on the fracture surface, and the boundaries of deformed particles are disappeared. Such phenomena can well explain the improvements of both ductility (elongation of about 3%) and strength (UTS of about 821 MPa). Similar with the studies on the CS fabrication of stainless-steel samples [51, 54], the post annealing treatment above the temperature of 1000 °C is necessary to improve the tensile properties by eliminating the particle boundary and promoting the metallurgical bonding. Furthermore, it can be noticed that the inter-particle cracks between WC and MS300 matrix are disappeared in the HT2 sample, which corresponds well with the observed diffusion layer. Such improved bonding between reinforcing WC particles and MS300 matrix can also facilitate the cohesive bonding with the WC/MS300 composite.

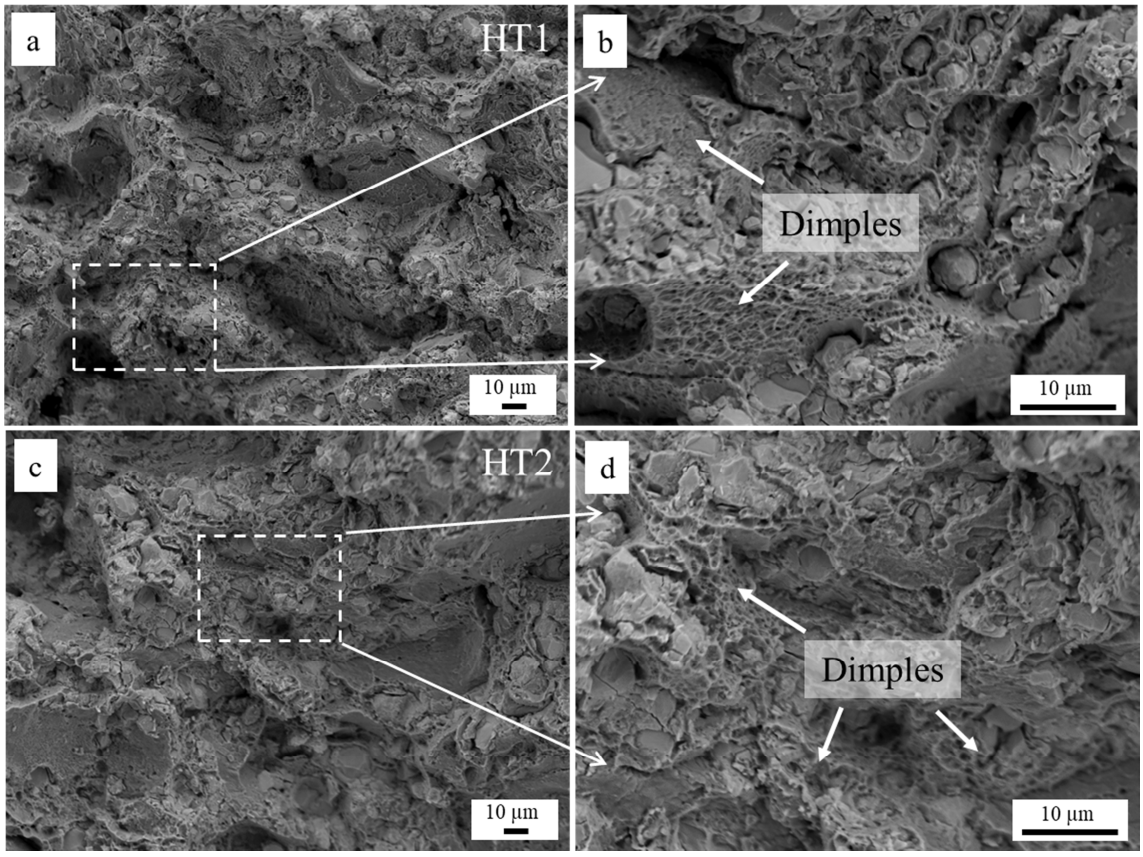

Fig. 19 Fracture surfaces of WC/MS300 composites at HT conditions, and the magnified views of corresponding boxed areas are given in the second column.

4. Conclusion

Based on the unique solid-state deposition process, the CS technique has been widely used to fabricate the MMCs samples as well as bulk materials. However, the low retainability of the reinforcement particles has always limited the maximization of mechanical properties of cold sprayed MMCs. In this work, WC reinforced maraging steel 300 composites was fabricated by high-pressure CS system. The reinforcement of WC particle can significantly improve the combination of wear resistance and mechanical strength. The main conclusions of this work are drawn as following:

1. Based on the reconstruction of X-ray computed tomography, the distribution of WC particles within the CS WC/MS300 composite samples can directly observed and analyzed. The volume fraction and distribution of equivalent diameter of the WC particle demonstrate that the higher retainability (85.4%) was obtained at higher propelling gas pressure (N_2, 5 MPa, 900 °C). Meanwhile, the solution-aging treatment result in the decrease of WC volume fraction and smoothing of WC shape.
2. Microstructure observation on WC evolution shows the thick diffusion layer was formed around the WC particle after solution-aging treatment, which can significantly improve the interfacial bonding. EBSD analysis shows nano-sized grains (less than 100 nm) were formed in the as-fabricated composite sample as a result of severe plastic deformation during deposition.
3. The as-fabricated samples with higher propelling gas pressure demonstrate a higher tensile strength and better wear resistance due to the more severe plastic deformation and higher WC retainability. It was found that the higher solution temperature (1000 °C) can lead to an enhanced cohesive bonding within the composite. The solution-aged composite shows an excellent wear resistance under the improved WC bonding and precipitation hardening.

Acknowledgement

The authors would like to acknowledge the support of High-level Leading Talent Introduction Program of GDAS (Grants No. 2016GDASRC-0204), GDAS' Project of Science and Technology Development (Grants No. 2018GDASCX-0945), International Cooperation Project (Grants No. 201807010013), the National Natural Science Foundation of China (No. 51604171, 51690162), the Shanghai Science and Technology Committee (No. 17JC1400602), the Young Scientists Fund of the National Natural Science Foundation of China 51701112. As one of the authors, Xingchen Yan, is grateful for the financial supports provided by the China Scholarship Council (No. 201504490031), the founds of Sciences Platform Environment and Capacity Building Projects of GDAS (2016GDASPT-0206, 2017GDASCX-0202, 2017GDASCX-0111, 2018GDASCX-0402 and 2018GDASCX-0111); Guangzhou Project of Science & Technology (201604016109, 201704030111); Guangdong province Science and Technology Plan Projects (2015B010122004, 2015B090920003 2016B070701020, 2016B090916003, 2017A070702016, 2017B030314122 and 2017A070701027); Guangdong Natural Science Foundation (2016A030312015). Guangzhou Science and Technology Program (201510010095).

Reference

[1] L.F. Vanswam, R.M. Pelloux, N.J. Grant, Fatigue Behavior of Maraging-steel 300, Metall Trans, 6 (1975) 45-54.

[2] K. Kempen, E. Yasa, L. Thijs, J.P. Kruth, J. Van Humbeeck, Microstructure and mechanical properties of Selective Laser Melted 18Ni-300 steel, Phys Procedia, 12, Part A (2011) 255-263.

[3] L. Sun, T.H. Simm, T.L. Martin, S. McAdam, D.R. Galvin, K.M. Perkins, P.A.J. Bagot, M.P. Moody, S.W. Ooi, P. Hill, M.J. Rawson, H.K.D.H. Bhadeshia, A novel ultra-high strength maraging steel with balanced ductility and creep resistance achieved by nanoscale β-NiAl and Laves phase precipitates, Acta Mater, 149 (2018) 285-301.

[4] P. Kürnsteiner, M.B. Wilms, A. Weisheit, P. Barriobero-Vila, E.A. Jägle, D. Raabe, Massive nanoprecipitation in an Fe-19Ni-xAl maraging steel triggered by the intrinsic heat treatment during laser metal deposition, Acta Mater, 129 (2017) 52-60.

[5] T. Hermann Becker, T. Hermann Becker, D. Dimitrov, D. Dimitrov, The achievable mechanical properties of SLM produced Maraging Steel 300 components, Rapid Prototyp J, 22 (2016) 487-494.

[6] D.D. Gu, W. Meiners, K. Wissenbach, R. Poprawe, Laser additive manufacturing of metallic components: materials, processes and mechanisms, Int Mater Rev, 57 (2012) 133-164.

[7] M.F. Ibrahim, H.R. Ammar, A.M. Samuel, M.S. Soliman, F.H. Samuel, On the impact toughness of Al-15 vol.% B4C metal matrix composites, Composites Part B, 79 (2015) 83-94.

[8] S. Yin, Y. Xie, J. Cizek, E.J. Ekoi, T. Hussain, D.P. Dowling, R. Lupoi, Advanced diamond-reinforced metal matrix composites via cold spray: Properties and deposition mechanism, Composites Part B, 113 (2017) 44-54.

[9] D. Gu, J. Ma, H. Chen, K. Lin, L. Xi, Laser additive manufactured WC reinforced Fe-based composites with gradient reinforcement/matrix interface and enhanced performance, Compos Struct, 192 (2018) 387-396.

[10] T. Rong, D. Gu, Q. Shi, S. Cao, M. Xia, Effects of tailored gradient interface on wear properties of WC/Inconel 718 composites using selective laser melting, Surf Coat Technol, 307, Part A (2016) 418-427.

[11] X. Yan, C. Huang, C. Chen, R. Bolot, L. Dembinski, R. Huang, W. Ma, H. Liao, M. Liu, Additive manufacturing of WC reinforced maraging steel 300 composites by cold spraying and selective laser melting, Surf Coat Technol, (2018).

[12] M.S. Lamana, A.G.M. Pukasiewicz, S. Sampath, Influence of cobalt content and HVOF deposition process on the cavitation erosion resistance of WC-Co coatings, Wear, 398-399 (2018) 209-219.

[13] P. Mi, H. Zhao, T. Wang, F. Ye, Sliding wear behavior of HVOF sprayed WC-(nano-WC-Co) coating at elevated temperatures, Mater Chem Phys, 206 (2018) 1-6.

[14] S. Zhou, J. Lei, X. Dai, J. Guo, Z. Gu, H. Pan, A comparative study of the structure and wear resistance of NiCrBSi/50 wt.% WC composite coatings by laser cladding and laser induction hybrid cladding, Int J Refract Met Hard Mater, 60 (2016) 17-27.

[15] Q. Ma, Y. Li, J. Wang, K. Liu, Investigation on cored-eutectic structure in Ni60/WC composite coatings fabricated by wide-band laser cladding, J Alloy Compd, 645 (2015) 151-157.
[16] H. Assadi, F. Gartner, T. Stoltenhoff, H. Kreye, Bonding mechanism in cold gas spraying, Acta Mater, 51 (2003) 4379-4394.
[17] S. Yin, X. Wang, X. Suo, H. Liao, Z. Guo, W. Li, C. Coddet, Deposition behavior of thermally softened copper particles in cold spraying, Acta Mater, 61 (2013) 5105-5118.
[18] S. Yin, M. Meyer, W. Li, H. Liao, R. Lupoi, Gas Flow, Particle Acceleration, and Heat Transfer in Cold Spray: A review, J Therm Spray Technol, 25 (2016) 874-896.
[19] M. Grujicic, J. Saylor, D. Beasley, W. DeRosset, D. Helfritch, Computational analysis of the interfacial bonding between feed-powder particles and the substrate in the cold-gas dynamic-spray process, Appl Surf Sci, 219 (2003) 211-227.
[20] C. Chen, Y. Xie, S. Yin, M.-P. Planche, S. Deng, R. Lupoi, H. Liao, Evaluation of the interfacial bonding between particles and substrate in angular cold spray, Mater Lett, 173 (2016) 76-79.
[21] C. Huang, W. Li, Y. Feng, Y. Xie, M.-P. Planche, H. Liao, G. Montavon, Microstructural evolution and mechanical properties enhancement of a cold-sprayed Cu Zn alloy coating with friction stir processing, Mater Charact, 125 (2017) 76-82.
[22] C. Chen, Y. Xie, R. Huang, S. Deng, Z. Ren, H. Liao, On the role of oxide film's cleaning effect into the metallurgical bonding during cold spray, Mater Lett, 210 (2018) 199-202.
[23] H. Assadi, H. Kreye, F. Gärtner, T. Klassen, Cold spraying – A materials perspective, Acta Mater, 116 (2016) 382-407.
[24] W. Li, K. Yang, S. Yin, X. Yang, Y. Xu, R. Lupoi, Solid-state additive manufacturing and repairing by cold spraying: A review, J. Mater. Sci. Technol., 34 (2017) 440-457.
[25] C. Chen, S. Gojon, Y. Xie, S. Yin, C. Verdy, Z. Ren, H. Liao, S. Deng, A novel spiral trajectory for damage component recovery with cold spray, Surf Coat Technol, 309 (2017) 719-728.
[26] W.Y. Li, R.R. Jiang, C.J. Huang, Z.H. Zhang, Y. Feng, Effect of cold sprayed Al coating on mechanical property and corrosion behavior of friction stir welded AA2024-T351 joint, Mater Des, 65 (2015) 757-761.
[27] X.-T. Luo, Y.-K. Wei, Y. Wang, C.-J. Li, Microstructure and mechanical property of Ti and Ti6Al4V prepared by an in-situ shot peening assisted cold spraying, Mater Des, 85 (2015) 527-533.
[28] P. Vo, E. Irissou, J.-G. Legoux, S. Yue, Mechanical and microstructural characterization of cold-sprayed Ti-6Al-4V after heat treatment, J Therm Spray Technol, 22 (2013) 954-964.
[29] A. Chaudhuri, Y. Raghupathy, D. Srinivasan, S. Suwas, C. Srivastava, Microstructural evolution of cold-sprayed Inconel 625 superalloy coatings on low alloy steel substrate, Acta Mater, 129 (2017) 11-25.
[30] X.-T. Luo, M.-L. Yao, N. Ma, M. Takahashi, C.-J. Li, Deposition behavior, microstructure and mechanical properties of an in-situ micro-forging assisted cold spray enabled additively manufactured Inconel 718 alloy, Mater Des, 155 (2018) 384-395.

[31] J. Pattison, S. Celotto, R. Morgan, M. Bray, W. O'Neill, Cold gas dynamic manufacturing: A non-thermal approach to freeform fabrication, Int J Mach Tool Manu, 47 (2007) 627-634.
[32] S. Yin, P. Cavaliere, B. Aldwell, R. Jenkins, H. Liao, W. Li, R. Lupoi, Cold spray additive manufacturing and repair: Fundamentals and applications, Addit Manuf, 21 (2018) 628-650.
[33] V.K. Champagne, The repair of magnesium rotorcraft components by cold spray, J Fail Anal Prev, 8 (2008) 164-175.
[34] D. Lioma, N. Sacks, I. Botef, Cold gas dynamic spraying of WC–Ni cemented carbide coatings, Int J Refract Met Hard Mater, 49 (2015) 365-373.
[35] N.M. Melendez, A.G. McDonald, Development of WC-based metal matrix composite coatings using low-pressure cold gas dynamic spraying, Surf Coat Technol, 214 (2013) 101-109.
[36] S.A. Alidokht, P. Manimunda, P. Vo, S. Yue, R.R. Chromik, Cold spray deposition of a Ni-WC composite coating and its dry sliding wear behavior, Surf Coat Technol, 308 (2016) 424-434.
[37] X.-T. Luo, C.-X. Li, F.-L. Shang, G.-J. Yang, Y.-Y. Wang, C.-J. Li, WC-Co Composite Coating Deposited by Cold Spraying of a Core-Shell-Structured WC-Co Powder, J Therm Spray Technol, 24 (2015) 100-107.
[38] S. Yin, E.J. Ekoi, T.L. Lupton, D.P. Dowling, R. Lupoi, Cold spraying of WC-Co-Ni coatings using porous WC-17Co powders: Formation mechanism, microstructure characterization and tribological performance, Mater Des, 126 (2017) 305-313.
[39] W. Li, H. Assadi, F. Gaertner, S. Yin, A Review of Advanced Composite and Nanostructured Coatings by Solid-State Cold Spraying Process, Crit Rev Solid State, (2018) 1-48.
[40] T.B. Torgerson, M.D. Harris, S.A. Alidokht, T.W. Scharf, S.M. Aouadi, R.R. Chromik, J.S. Zabinski, A.A. Voevodin, Room and elevated temperature sliding wear behavior of cold sprayed Ni-WC composite coatings, Surf Coat Technol, 350 (2018) 136-145.
[41] ASTM E8 / E8M-16a, Standard Test Methods for Tension Testing of Metallic Materials, ASTM International, West Conshohocken, PA, 2016, www.astm.org.
[42] S. Tammas-Williams, H. Zhao, F. Léonard, F. Derguti, I. Todd, P.B. Prangnell, XCT analysis of the influence of melt strategies on defect population in Ti–6Al–4V components manufactured by Selective Electron Beam Melting, Mater Charact, 102 (2015) 47-61.
[43] J. Mutua, S. Nakata, T. Onda, Z.-C. Chen, Optimization of selective laser melting parameters and influence of post heat treatment on microstructure and mechanical properties of maraging steel, Mater Des, 139 (2018) 486-497.
[44] I. Maskery, N.T. Aboulkhair, M.R. Corfield, C. Tuck, A.T. Clare, R.K. Leach, R.D. Wildman, I.A. Ashcroft, R.J.M. Hague, Quantification and characterisation of porosity in selectively laser melted Al–Si10–Mg using X-ray computed tomography, Mater Charact, 111 (2016) 193-204.
[45] K. Yang, W. Li, X. Guo, X. Yang, Y. Xu, Characterizations and anisotropy of cold-spraying additive-manufactured copper bulk, J. Mater. Sci. Technol., (2018).

[46] K. Kang, H. Park, G. Bae, C. Lee, Microstructure and texture of Al coating during kinetic spraying and heat treatment, J Mater Sci, 47 (2012) 4053-4061.
[47] Y. Zou, W. Qin, E. Irissou, J.-G. Legoux, S. Yue, J.A. Szpunar, Dynamic recrystallization in the particle/particle interfacial region of cold-sprayed nickel coating: Electron backscatter diffraction characterization, Scr Mater, 61 (2009) 899-902.
[48] Y.-K. Wei, Y.-J. Li, Y. Zhang, X.-T. Luo, C.-J. Li, Corrosion resistant nickel coating with strong adhesion on AZ31B magnesium alloy prepared by an in-situ shot-peening-assisted cold spray, Corros Sci, 138 (2018) 105-115.
[49] C. Lee, J. Kim, Microstructure of Kinetic Spray Coatings: A Review, J Therm Spray Technol, 24 (2015) 592-610.
[50] R. Huang, M. Sone, W. Ma, H. Fukanuma, The effects of heat treatment on the mechanical properties of cold-sprayed coatings, Surf Coat Technol, 261 (2015) 278-288.
[51] P. Coddet, C. Verdy, C. Coddet, F. Debray, F. Lecouturier, Mechanical properties of thick 304L stainless steel deposits processed by He cold spray, Surf Coat Technol, 277 (2015) 74-80.
[52] J.J.J.o.m.s.l. Kováčik, Correlation between Young's modulus and porosity in porous materials, 18 (1999) 1007-1010.
[53] X. Yan, S. Yin, C. Chen, C. Huang, R. Bolot, R. Lupoi, M. Kuang, W. Ma, C. Coddet, H. Liao, M. Liu, Effect of heat treatment on the phase transformation and mechanical properties of Ti6Al4V fabricated by selective laser melting, J Alloy Compd, 764 (2018) 1056-1071.
[54] X.-M. Meng, J.-B. Zhang, W. Han, J. Zhao, Y.-L. Liang, Influence of annealing treatment on the microstructure and mechanical performance of cold sprayed 304 stainless steel coating, Appl Surf Sci, 258 (2011) 700-704.